

An in-situ prepared covalent sulfur-carbon composite electrode for high performance room-temperature sodium-sulfur batteries

Jie Yan,^{a,b} Wei Li,^b Ruxing Wang,^a Pingyuan Feng,^b Mao Jiang,^b Jing Han,^b Shengling Cao,^b Zhuchan Zhang,^b Kangli Wang,^{*a} and Kai Jiang^{*a}

^a School of Electrical and Electronic Engineering, Huazhong University of Science and Technology, Wuhan, Hubei, China 430074.

^b School of Materials Science and Engineering, Huazhong University of Science and Technology, Wuhan, Hubei, China 430074.

E-mail: kjiang@hust.edu.cn, klwang@hust.edu.cn

Supporting information

Experimental section

Synthesis of covalent-SC

The covalent sulfur-carbon (covalent-SC) composite was prepared by a simple, novel and one-step wet chemical solvothermal reaction. Briefly, 1 g of commercial red phosphorus (RP, Alfa Aesar, amorphous, 98.9%) without purification and 100 mL of carbon disulfide (CS₂, Sinopharm Chemical Reagent Co., Ltd) were added into a 200 mL vessel (hastelloy alloy) with temperature and pressure detection and then heated at different temperatures (250, 300, 400 and 500 °C) for 12 h. The covalent-SC

composites were obtained by washing with CS₂ and absolute ethyl alcohol for three times respectively and then dried at 70 °C for 12 h in a vacuum.

Materials characterization

The morphology of covalent-SC was observed by Field Emission Scanning Electron Microscopy (FESEM, JEM7600F) and Transmission electron microscope (TEM, JEOL2100). The structure feature of covalent-SC was collected by the PANalytical Multi-Purpose Diffractometer equipped with a Cu K α radiation ($\lambda=0.15406$ nm). The Raman spectrum of covalent-SC was collected on the LabRAM HR800 Raman system with a Raman light source of 532 nm. The Fourier transformed infrared (FTIR) spectrum was measured on the Bruker VERTEX 70 FTIR spectrometer. The XPS spectra of covalent-SC was obtained on the AXIS-ULTRA DLD spectrometer with a monochromatic Al K α X-ray source. The Tristar II 3020 instrument was used to characterize the nitrogen adsorption and desorption isotherms of covalent-SC at 77 K. The thermogravimetric analysis (TGA) was carried out to obtain the weightless information of covalent-SC under N₂ atmosphere in the Netzsch Instruments (STA 449 F5). The composition of covalent-SC was determined by using a Vario Micro cube elemental analyzer (EA).

Electrochemical measurements

The electrochemical performance was evaluated by assembling 2025 coin-type cell in the glove box filled with argon (H₂O < 0.1ppm, O₂ < 0.1ppm). To fabricate the working electrode, the active materials, Ketjenblack and PVDF were grinded in the agate mortar for 20min with a mass ratio of 7:2:1, then grinded in the NMP for 10min

to obtain a homogeneous slurry. The obtained slurry was uniformly pasted on the copper foil and dried under vacuum at 80 °C for 24 h, then cut into small slices (diameter~10mm). The mass loading of slice was 1.4-1.7 mg. Then, sodium metal was applied as anode, 1M NaClO₄ in ethylene carbonate(EC)/ diethyl carbonate(DEC) (1/1, V/V) with 5 wt% fluoroethylene carbonate (FEC) and glass fiber were used as electrolyte and separator respectively. The galvanostatic charge and discharge tests were measured on the battery testing system (LAND Electronic Co., China) under different interval of voltage range from 0.01-3 V to 1.0-3.0 V. The CV measurements were carried out on the electrochemical workstation (CHI 604E, china) with different scan rates (0.1~5 mV s⁻¹). The electrochemical impedance spectra (EIS) were obtained by the electrochemical workstation (CHI 604E, china) with the frequency range from 100000 to 0.01 Hz.

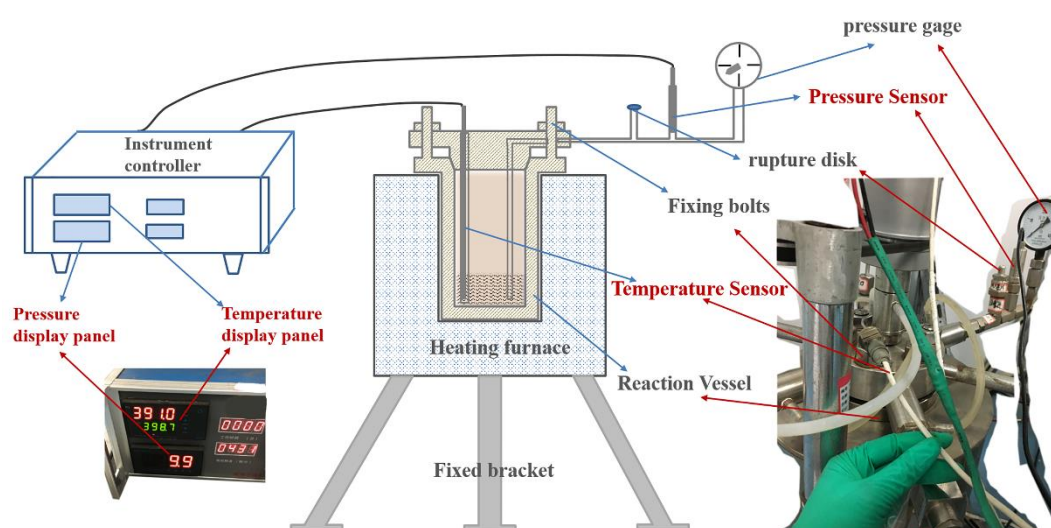


Figure S1. Schematic and figure of the vessel used for the high-temperature reactions.

Caution: as shown in Figure S1, the vessel should be fastened by 8 nuts and screwed to 200 N with a torque wrench (75 cm long). The reaction temperature and pressure

can be monitored by the temperature and pressure sensors and displayed on the controller panel. It is important to note that pressure and temperature should not exceed the design range (here the maximum temperature and pressure are 550 °C and 25 Mpa, respectively). In addition, the volume of solvent should not exceed half of the volume of vessel, and it cannot be used for the reaction of corrosive system.

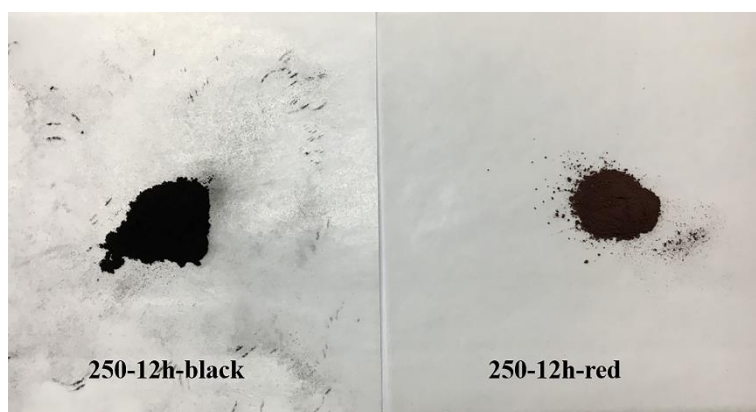


Figure S2. The products (black and dark red) obtained at 250 °C for 12h.

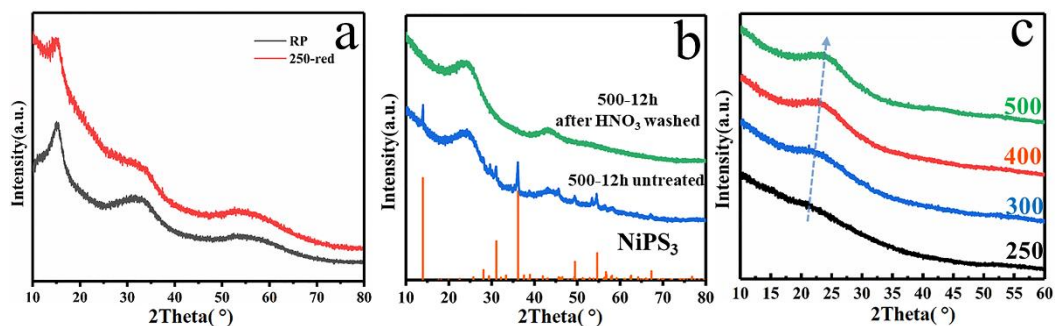


Figure S3. XRD patterns of red phosphorus and the dark red products obtained at 250 °C (a), XRD patterns of the product obtained at 500 °C (b), XRD patterns of the dark products obtained at different temperatures (250, 300, 400 and 500 °C) (c).

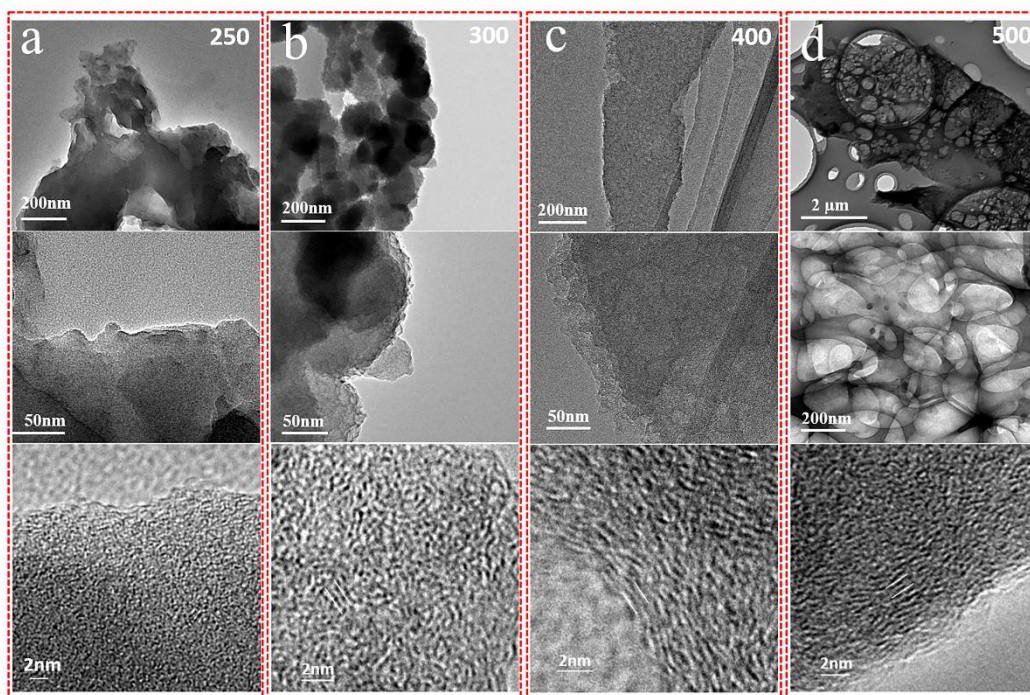


Figure S4. TEM and HRTEM images of the covalent-SC composites obtained at 250 °C (a), 300 °C (b), 400 °C (c), 500 °C (d).

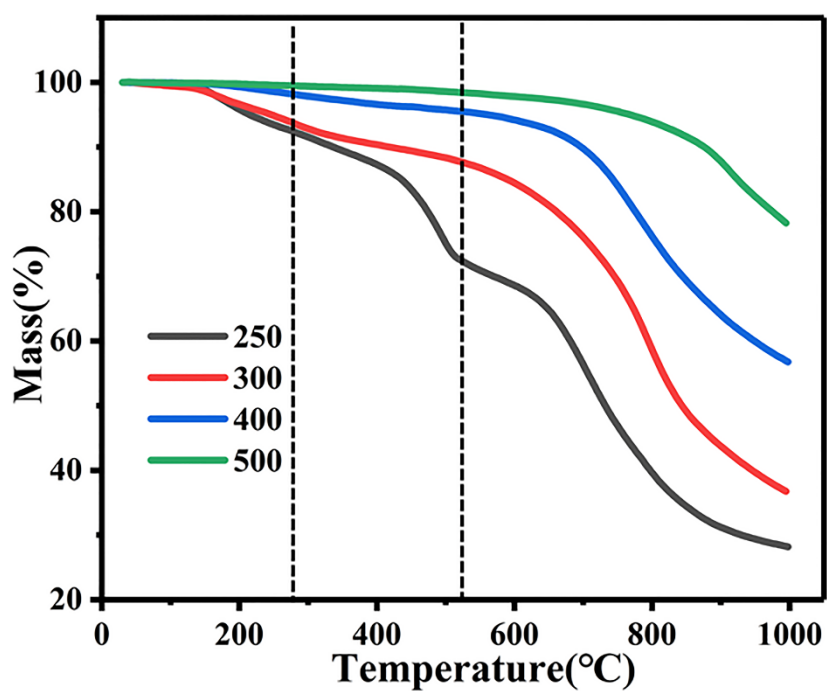


Figure S5. TG curves under N₂ atmosphere of the covalent-SC composites obtained at different temperatures.

There is a significant weight loss between 280 and 520 °C in the black composite

obtained at 250 °C, corresponding to the cleavage of P-S functional groups. This weight loss content decreases with the increase of synthetic temperature and becomes extremely small at 400 °C, indicating that the synthetic reactions are completed.

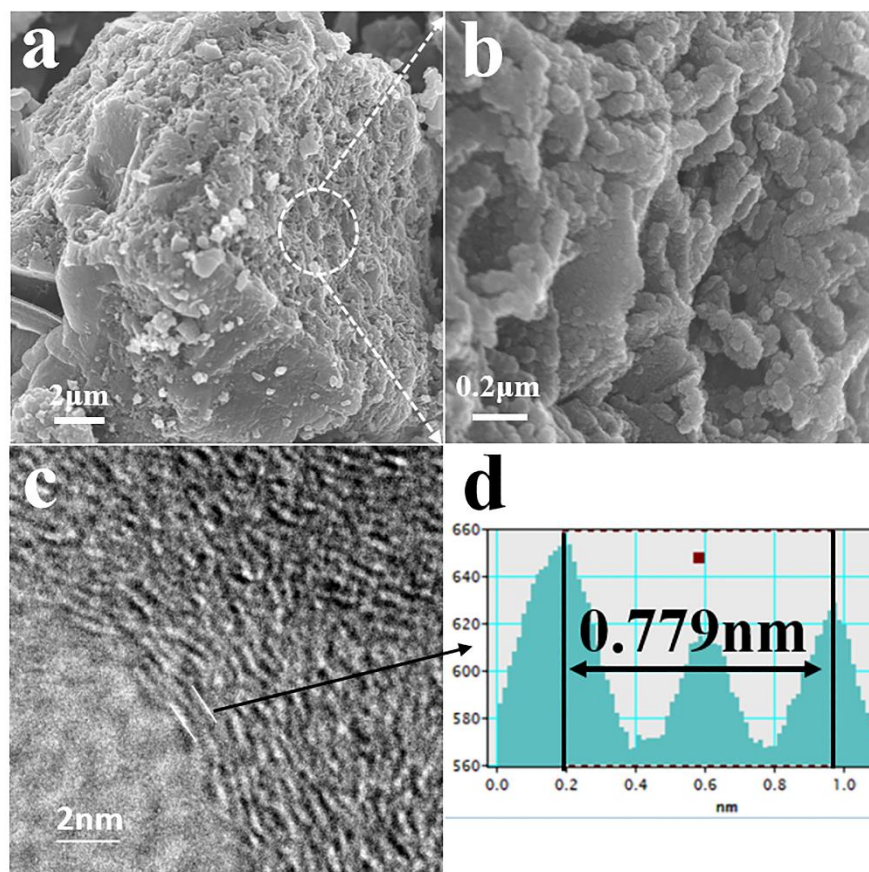


Figure S6. FESEM images (a, b), high resolution TEM image (c) and the corresponding interlayer spacing (d) of the covalent-SC obtained at 400 °C.

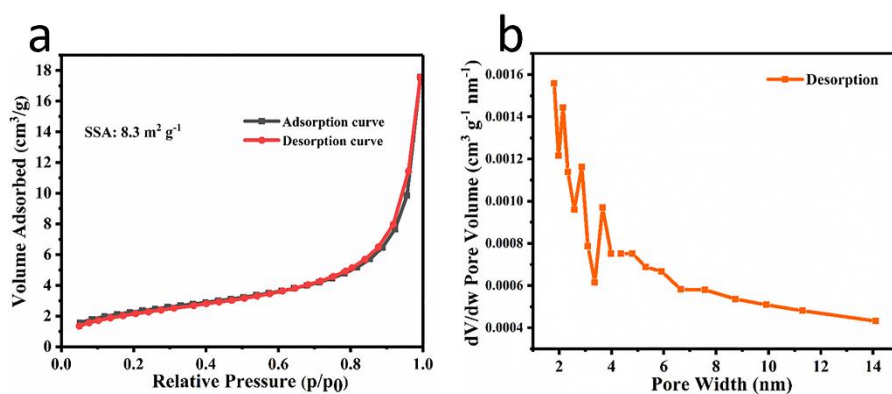


Figure S7. N₂ adsorption-desorption isotherms (a) and pore distribution (b) of the covalent-SC.

covalent-SC obtained at 400 °C.

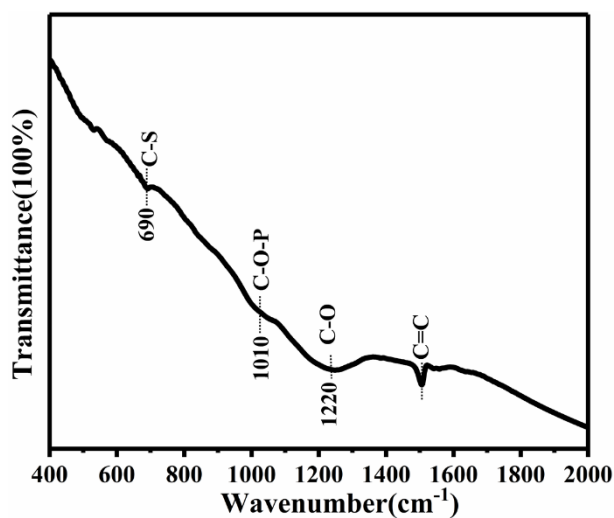


Figure S8. FTIR spectrum of covalent-SC.

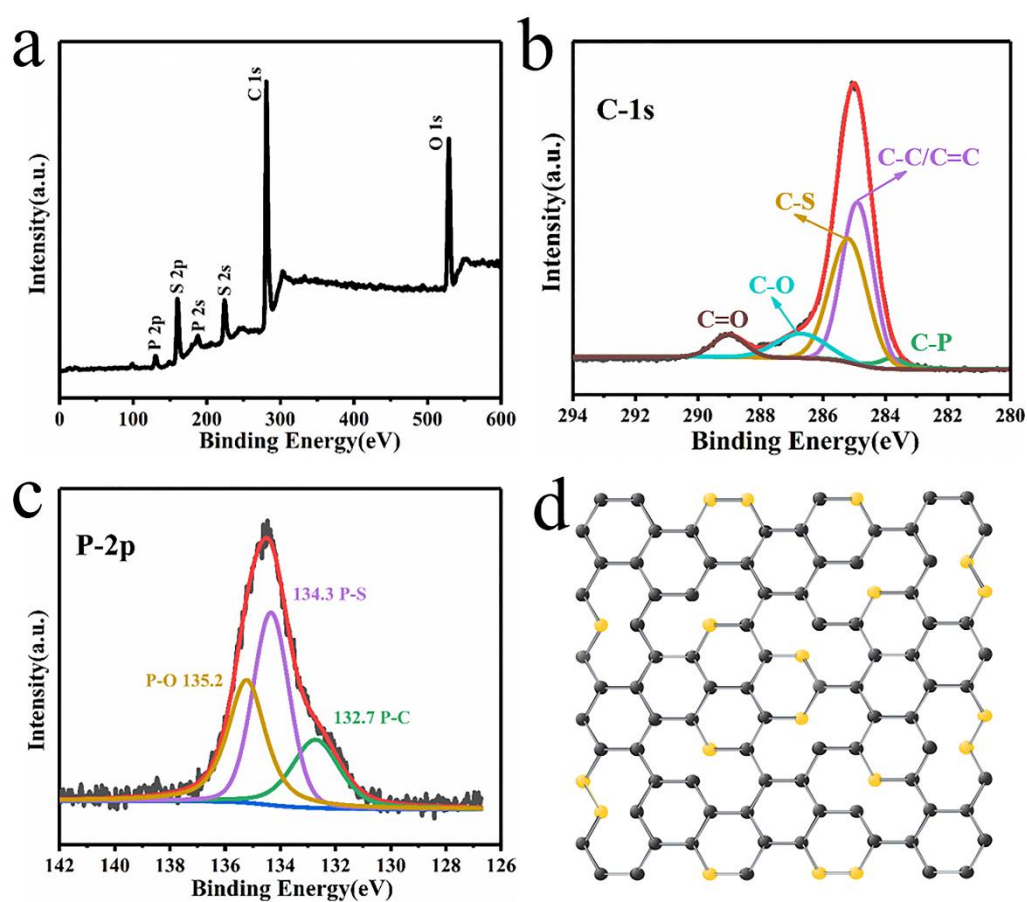


Figure S9. Survey XPS spectrum (a), high resolution XPS spectra of C 1s (b), P 2p (c) and a rational structure of covalent-SC (d).

The interaction of sulfur with carbon matrix can be further identified by XPS. As shown in Figure S9a, five predominant peaks at about 127, 165, 228, 285 and 534 eV observed in the XPS survey spectrum of covalent-SC correspond to the P 2p, S 2p, S2s, C 1s and O 1s characteristic peaks, respectively. The detection of element phosphorus here is due to the fact that a small portion of P (2.31 wt%) inevitable remains in the carbon structure during the desulfurization process. The high resolution C 1s spectrum (Figure S9b) can be deconvoluted into five peaks at 289.0, 286.7, 285.2, 284.9, and 283.8 eV, which correspond to C=O, C-O, C-S, C-C/C=C and C-P bonds respectively, [23-25] indicating that S and a small quantity of P are incorporated into carbon matrix. The P 2p spectrum of covalent-SC (Figure S9c) can be fitted into three peaks. The binding energies of 134.3 and 132.7 eV are assigned to P-S and P-C bonds, while peak at 135.2 eV is attributed to P-O bond due to the surface oxidation of RP,[26,27] suggesting that slight phosphorus is incorporated into carbon matrix. It should be mentioned here that the incorporation of phosphorus into carbon structure can improve the electronic conductivity of the materials and boost the adsorption of the Na⁺ ions, as revealed in previous reports,[23,28] which may promote the combination of sulfur and Na⁺ ions and enhance the electrochemical performance. A rational structure of covalent-SC can be illustrated in Figure S9d. The covalent sulfur uniformly distributes among the matrix (including the boundary and interior regime) at molecular level with C-S bonds, thus keeping intimately electrical contact with carbon. Furthermore, this short-chain covalent sulfur may be directly converted into low order sulfide without dissolution problem, which is expected to achieve a high

electrochemical performance. In addition, it should be noted that boundary sulfur may be more active than interior sulfur due to the higher energy of boundary atoms. Moreover, in a layered structure, an energy barrier for intercalating into the interlayer must be overcome to react with interior atoms, which further increases the resistance of the reaction.

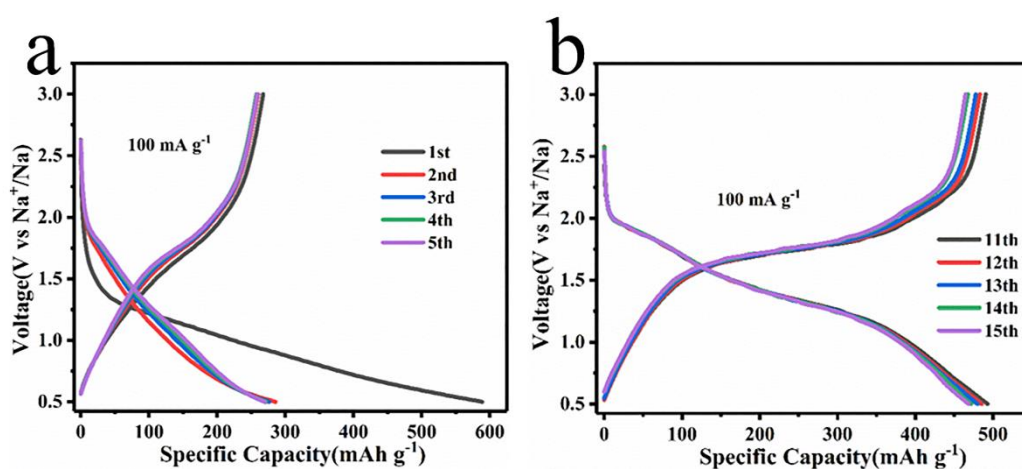


Figure S10. Voltage profiles of covalent-SC electrode cycled in the voltage of 0.5-3.0 V at 100 mA/g_{total} without activation (a) and after an activated process in the voltage of 0.01-3.0 V (b).

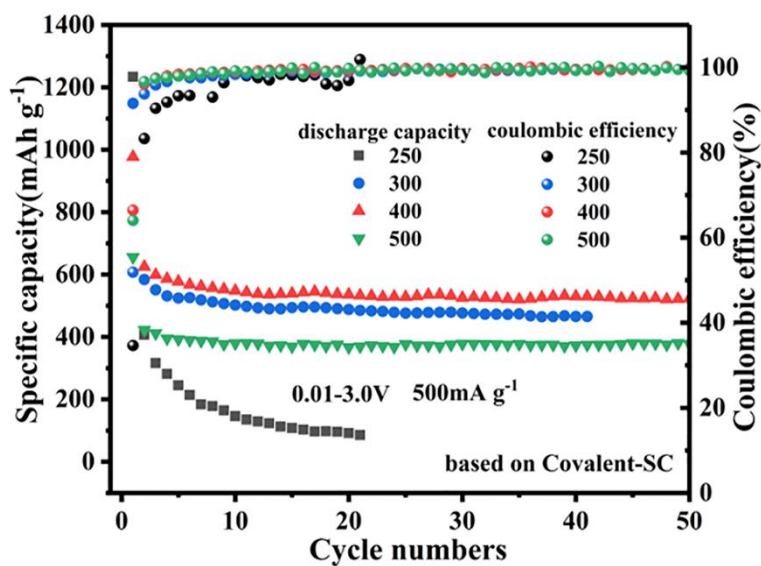


Figure S11. Cycle performance of covalent-SC composites obtained at different

temperatures.

Obviously, the covalent-SC obtained at 400 °C exhibits the best performance including high capacity and recyclability.

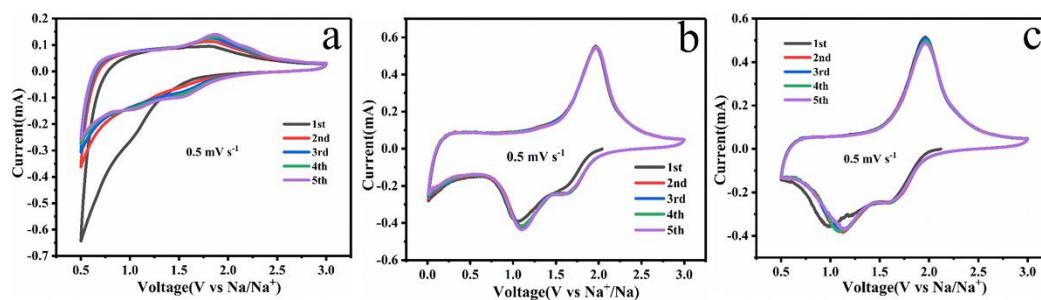


Figure S12. CV curves of the covalent-SC electrode in the voltage of 0.5-3.0 V (a), 0.01-3.0 V after a gradually reduced low-cutoff voltage (b), 0.5-3.0 V after a fully activated process (c) at the scan rate of 0.5 mV s⁻¹.

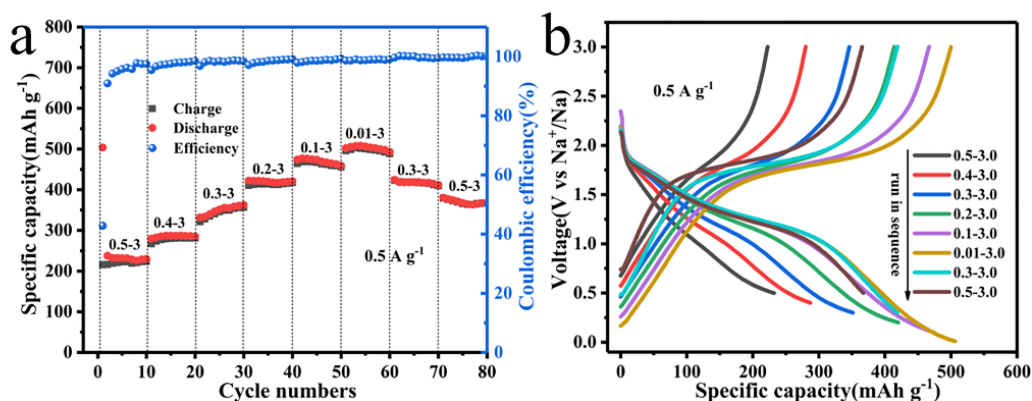


Figure S13. Cycling performance of the covalent-SC electrode with gradually reduced low-cutoff voltage (0.5 to 0.01 V) (a) and the corresponding voltage profiles (b) at 500 mA/g_{total}.

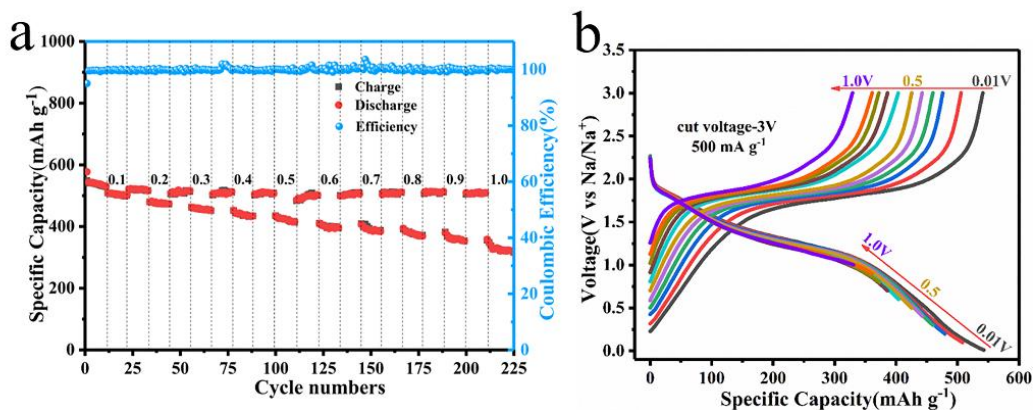


Figure S14. Cycling performance of the covalent-SC electrode with a gradually increased low-cutoff voltage (0.1-1.0 V) after a fully activated process in the voltage range of 0.01-3 V (a) and the corresponding voltage profiles at 500 mA/g_{total} (b).

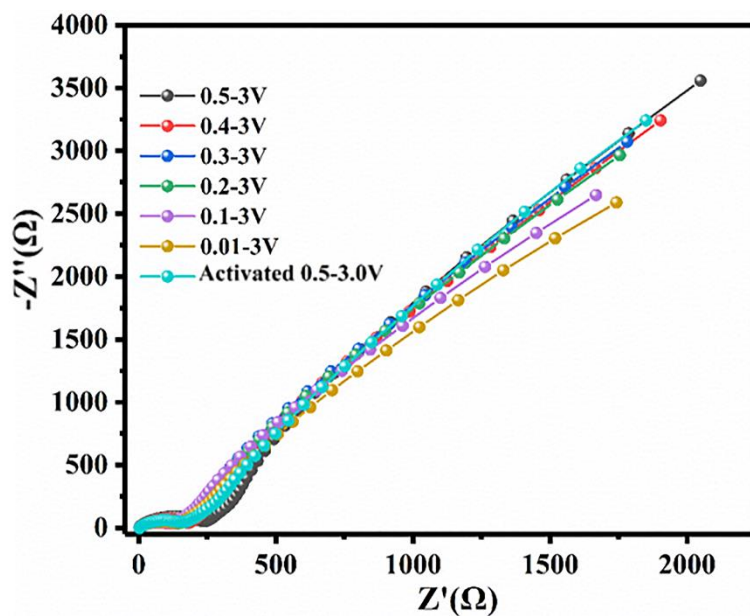


Figure S15. Electrochemical impedance spectra of the covalent-SC electrode at fully-charged states after 5 cycles in the different voltage ranges.

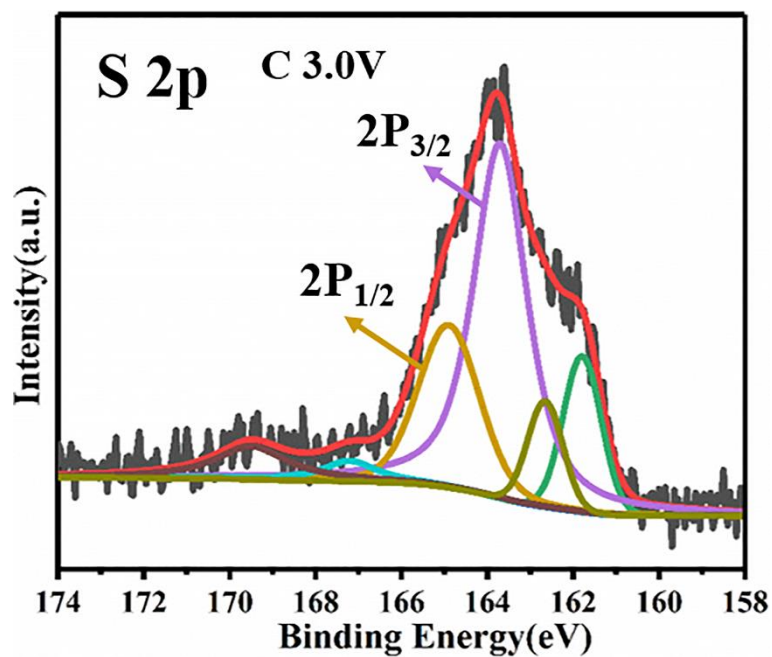


Figure S16. *Ex situ* high resolution XPS spectrum of S 2p of the covalent-SC electrode at 3.0 V in the first cycle.

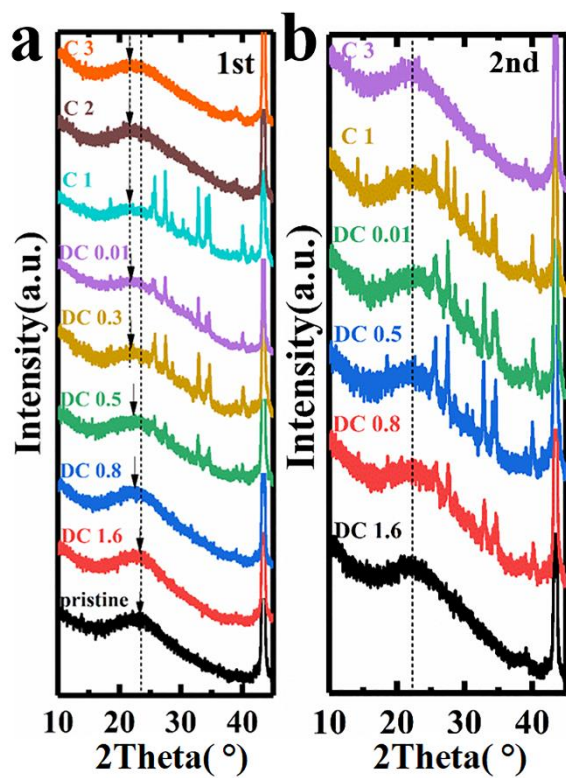


Figure S17. *Ex-XRD* patterns of covalent-SC electrodes at various intermediate states in the first (a) and second cycles (b).

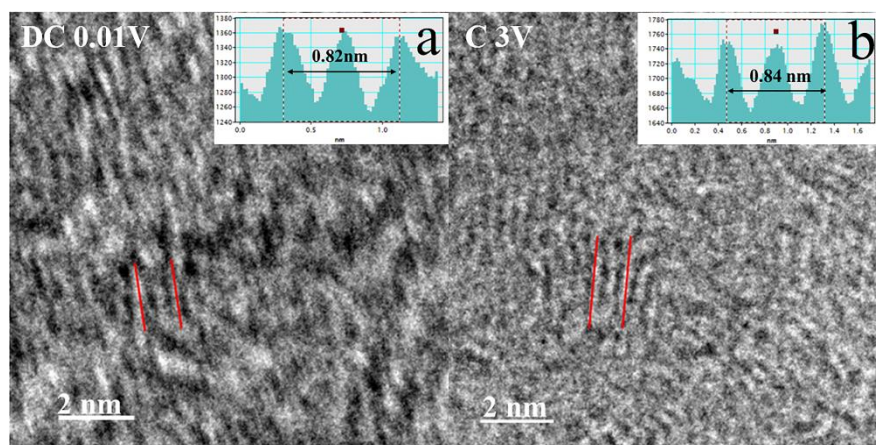


Figure S18. *Ex situ* HRTEM images of covalent-SC at fully discharged state of 0.01 V (a) and fully charged state of 3.0 V (b) in the first cycle. The insets are the corresponding interlayer distances, respectively.

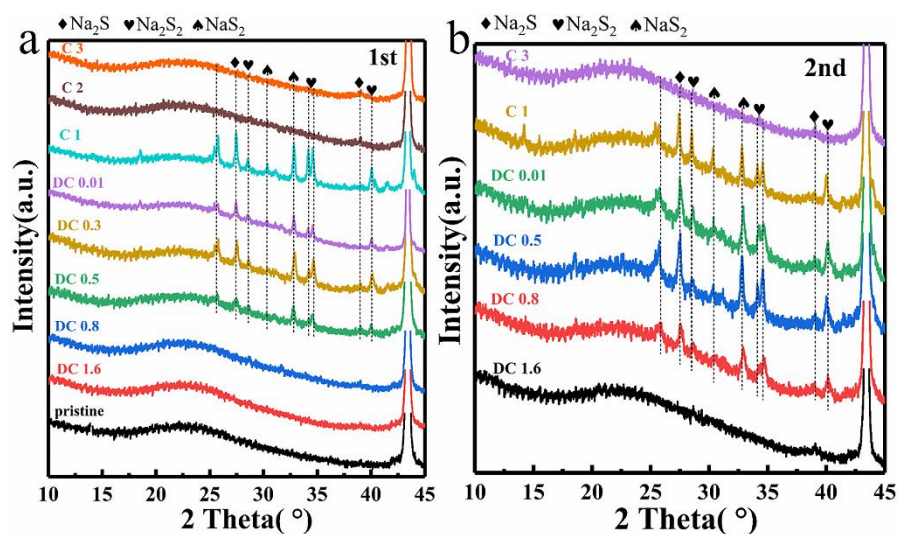


Figure S19. *Ex*-XRD patterns of covalent-SC electrodes at various intermediate states in the first (a) and second cycles (b).

As can be seen in the Figure S19a, the peaks belonging to Na_2S_x ($x=1\sim4$) do not appear with weak intensity until discharged to 0.5 V in the first cycle, while in the second discharge process, they appear at 0.8 V furthermore with extremely strong intensity at 0.5 V, indicating that Na^+ could access into the interlayers to react with

covalent sulfur owing to the enlarged d -spacing in the first cycle (Figure S19b). Such adsorption-like intercalated behavior may make the reaction between the interior sulfur and sodium ions exhibit a pseudocapacitive characteristic which is revealed in Figure S26, boosting an enhanced rate capability. In addition, no characteristic peaks belonging to element sulfur can be found in the electrode charged to 3.0 V, indicating the absence of element sulfur (Figure S20).

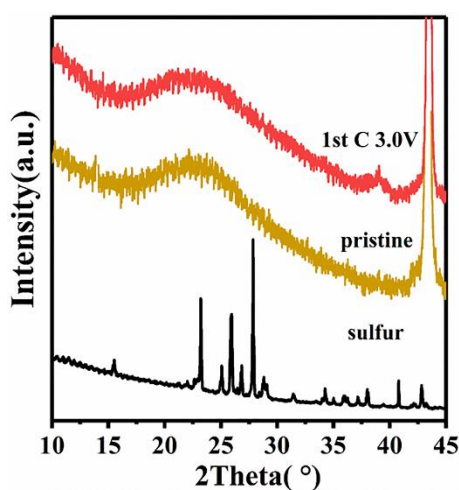


Figure S20. XRD patterns of pure sulfur and covalent-SC electrodes at different states.

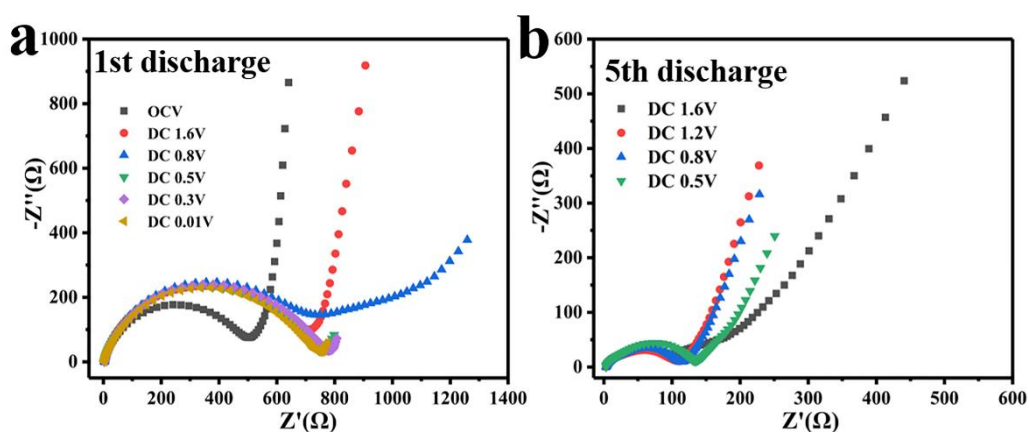


Figure S21. EIS of the covalent-SC electrode at different intermediate states in the (a) first cycle and (b) fifth cycle.

Obviously, the charge transfer resistance of discharge process in the fifth cycle is significantly reduced after the activation process in the first cycle, indicating the energy barrier and resistance of intercalation of Na^+ ions are reduced owing to the enlarged layer spacing.

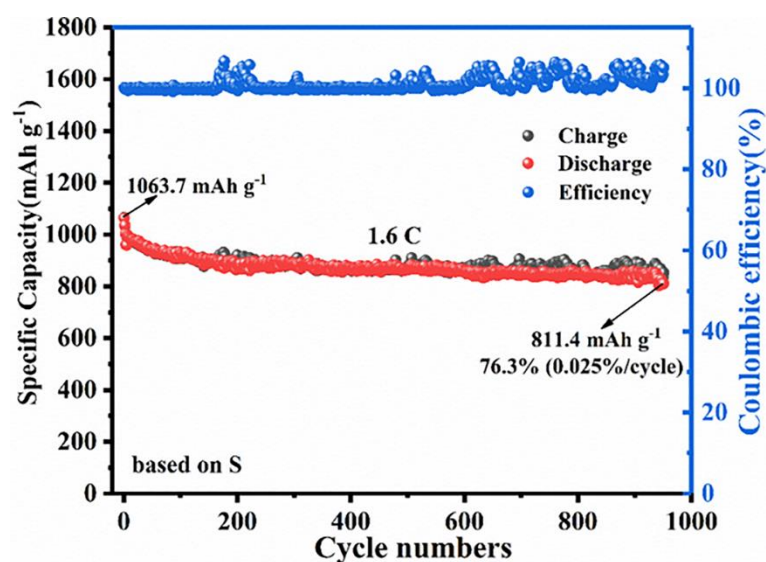


Figure S22. Cycling performance and coulombic efficiency of the activated covalent-SC electrode at 1.6 C.

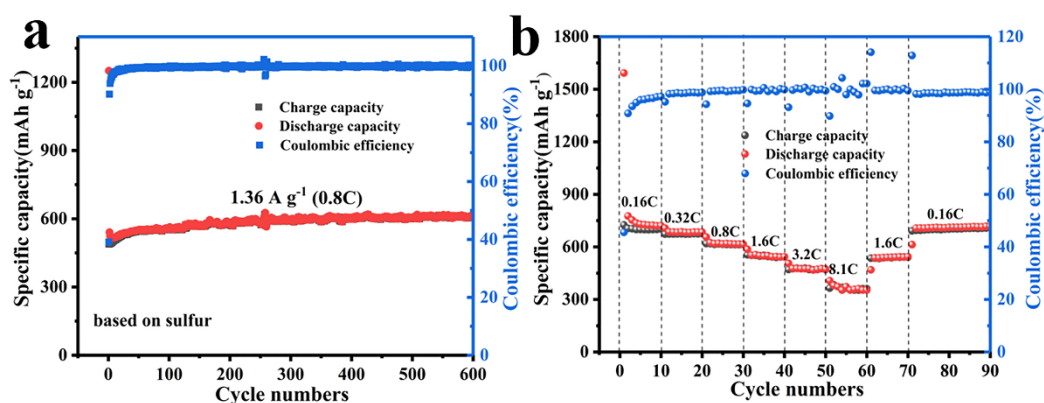


Figure S23. Electrochemical performance of covalent-SC electrodes directly cycled from 0.5 V to 3.0 V without activation for RT-Na/S batteries. Long cycle performance and the corresponding coulombic efficiency at 0.8 C (a), rate performance (b).

As shown in Figure 5a and Figure S23a, the activated covalent-SC electrode delivers

an initial discharge capacity of 1069.9 mAh g⁻¹ at 0.8 C, and retains a reversible capacity of 888.9 mAh g⁻¹ after 600 cycles, far higher than that of electrode without activation (607.0 mAh g⁻¹ after 600 cycles). Moreover, the activated covalent-SC electrode exhibits high discharge capacities of 1336, 1140, 1016, 940, 843 and 700 mAh g⁻¹ at 0.16C, 0.32C, 0.8C, 1.6C, 3.2C and 8.1C, respectively, also much higher than that of unactivated electrode (730, 686, 618, 549, 475 and 361 mAh g⁻¹ at 0.16C, 0.32C, 0.8C, 1.6C, 3.2C and 8.1C, respectively) as revealed in Figure S23b. These results demonstrate the significant enhancement of electrochemical performance by the activation process.

Table S1. A cyclic performance comparison of sulfur-carbon cathodes reported in the previous literatures with the activated covalent-SC electrode developed in this work.

Material	Current density (mA g ⁻¹)	Cycle number	Initial capacity (mAh g ⁻¹)	Reversible capacity (mAh g ⁻¹)	Capacity retention	Journal (year)
SC-BDSA[1]	250 2500	200 1000	1057 696	785 452	74% 65%	Adv. Energy Mater.(2019)
S@MPCF[2]	167 1670	200 500	1635 --	927 581	77.7% --	Nat. Commun. (2018)
S@Con-HC[3]	100	600	1081	508	47.0%	Nat. Commun. (2018)
S@Fe-HC[4]	100	1000	1023	394	38.5%	Angew. Chem. (2019)
CSB@TiO ₂ [5]	500 1000	400 1400	1020 --	611 525	59.9% --	Adv. Funct. Mater. (2018)
CNT-ZIF8-S[6]	837	500	603	410	68.0%	J. Mater. Chem. A (2019)
S-TiC ₂ Tx[7]	837 3350	200 500	970 821.7	690.3 577.1	71.2% 70.2%	ACS nano (2019)
I-S@pPAN[8]	167 837	100 500	1787 994	850 768	47.6% 77.3%	Chem. Commun. (2019)
RGO-VO ₂ -S[9]	335	200	876.4	400	45.6%	Chem. Eng. J (2020)
Se _{0.08} S _{0.92} @pPAN[10]	200 400	200 500	1100 1185	850 770	77.3% 65.0%	J. Mater. Chem. A (2019)
NiS ₂ @NPCTs/S[11]	1000	750	960	401	41.8%	Nat. Commun. (2019)
pPAN/SeS ₂ [12]	100 1000	50 400	1530 1043	835 800	54.6% 76.7%	Sci. Adv. (2018)
MCPS[13]	167	100	866	600	69.3%	Nat. Commun. (2016)
SPAN[14]	335 1675	100 300	-- --	1070 788	-- --	Energy Storage Materials (2019)
S@C[15]	167	250	1524	450	30%	Nano letters (2017)
covalent-SC[This work]	270 1355 2710	340 600 950	1336 1070 1064	1022 889 811	76.5% 83.1% 76.3%	N/A

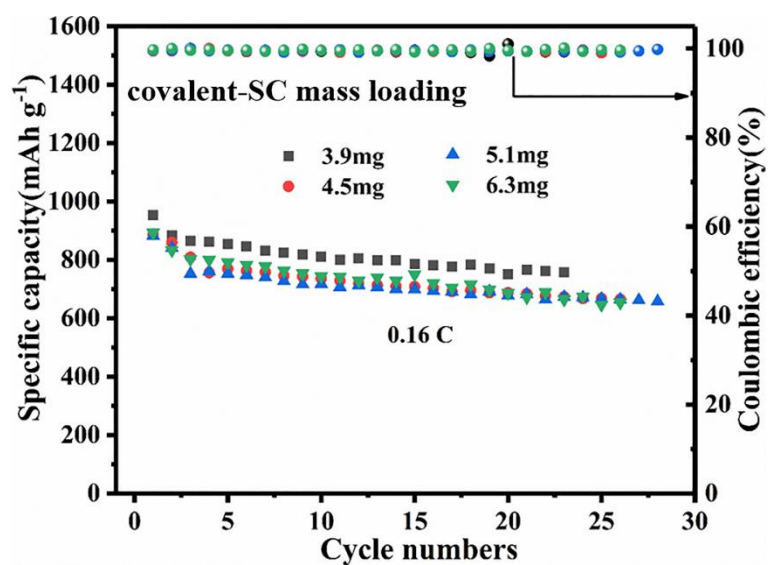


Figure S24. The effect of different active mass loadings on the capacities.

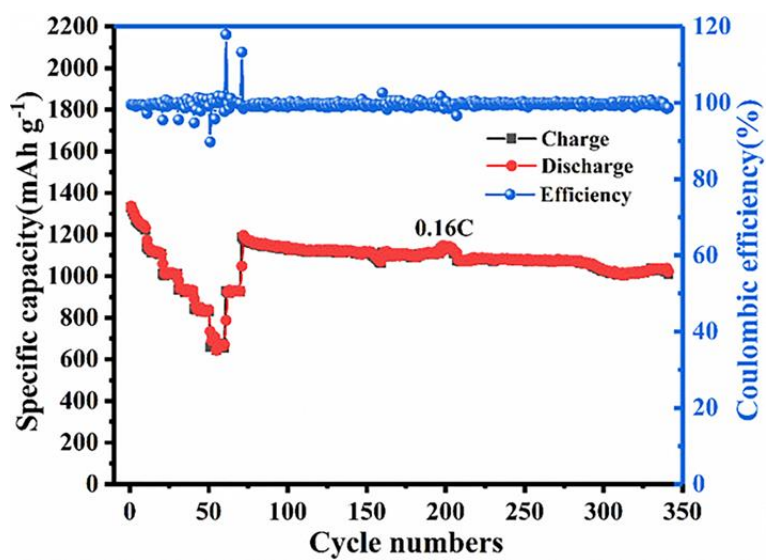


Figure S25. Cycling performance of the activated covalent-SC electrode in the voltage of 0.5-3.0 V at 0.16C.

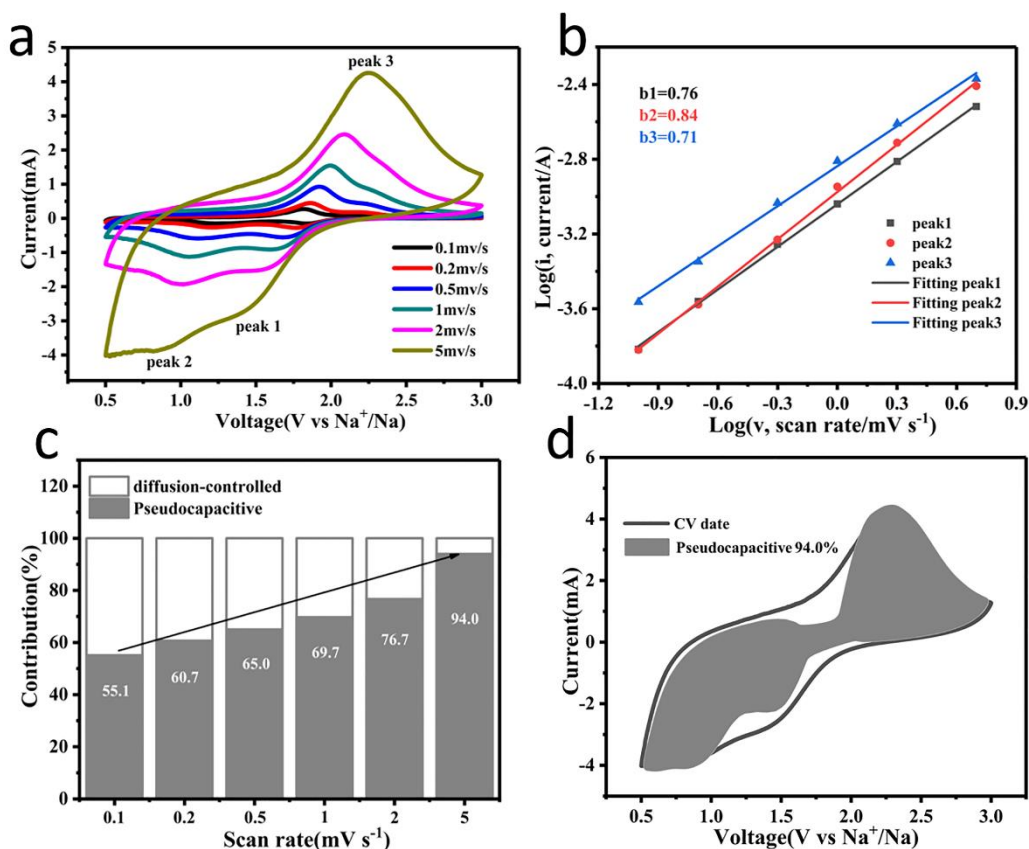


Figure S26. The kinetic analysis of the activated covalent-SC electrode. CV curves (a) at various scan rates (0.1 to 5 mV s^{-1}), the fitted lines of $\log(v)$ - $\log(i)$ applied to estimate the b -values (b), Calculated pseudocapacitive contributions at various scan rates (c) and the pseudocapacitive current contribution at 5 mV s^{-1} (d).

To further understand the excellent rate capability of covalent-SC, the CV curves at various scan rates from 0.1 to 5 mV s^{-1} (Figure S26a) are performed to analyze the reaction kinetics based on the equation 1:

$$i = av^b$$

Where a and b are adjustable values, and v is the scan rate. When the b value closes to 0.5 , it indicates that the reaction is controlled by the diffusion process. While the b value approaches 1 , it represents that the reaction is dominated by capacitive process.^[16-19] The b value can be calculated by linearly fitting the $\log(v)$ - $\log(i)$ curve.

As shown in Figure S26b, the b values for two anodic peaks (peak1 and peak2) and cathodic peak (peak3) are 0.76, 0.84 and 0.71, respectively, indicating the reaction is dominated by capacitive process. The contribution of capacitive capacity can be further calculated by investigating the current response to scan rate with the equation 2:

$$i(V) = k_1 v + k_2 v^{1/2}$$

where $i(V)$ is the current response at a certain voltage which consists of the pseudocapacitive current ($k_1 v$) and the diffusion-controlled current ($k_2 v^{1/2}$).^[20-22] The pseudocapacitive contribution can be quantitatively determined by solving for the values of k_1 and k_2 at each voltage. As shown in Figure S26c, the pseudocapacitive contribution accounts for 55.1% of the total capacity at the scan rate of 0.1 mV s⁻¹. When the scan rate increases from 0.1 to 5 mV s⁻¹, the pseudocapacity contribution ratio increases from 55.1% to 94.0% (Figure S26d), indicating that the pseudocapacitive behavior is dominated and responsible for the fast kinetics of covalent-SC electrode. Furthermore, this dominated pseudocapacitance contributed by the rapidly binding of boundary sulfur with Na⁺ and the reaction between interior sulfur and intercalated Na⁺ with adsorption-like behavior.

Reference

1. Wu, T.; Jing, M.; Yang, L.; Zou, G.; Hou, H.; Zhang, Y.; Zhang, Y.; Cao, X.; Ji, X. Controllable Chain-Length for Covalent Sulfur–Carbon Materials Enabling Stable and High-Capacity Sodium Storage. *Adv. Energy Mater.* **2019**, 9 (9),

1803478. DOI: 10.1002/aenm.201803478.

2. Xu, X.; Zhou, D.; Qin, X.; Lin, K.; Kang, F.; Li, B.; Shanmukaraj, D.; Rojo, T.; Armand, M.; Wang, G. A Room-Temperature Sodium–Sulfur Battery with High Capacity and Stable Cycling Performance. *Nat. Commun.* **2018**, 9 (1), 1–12. DOI: 10.1038/s41467-018-06443-3.
3. Zhang, B. W.; Sheng, T.; Liu, Y. D.; Wang, Y. X.; Zhang, L.; Lai, W. H.; Wang, L.; Yang, J.; Gu, Q. F.; Chou, S. L.; et al. Atomic Cobalt as an Efficient Electrocatalyst in Sulfur Cathodes for Superior Room-Temperature Sodium-Sulfur Batteries. *Nat. Commun.* **2018**, 9 (1), 1-11. DOI: 10.1038/s41467-018-06144-x.
4. Zhang, B. W.; Sheng, T.; Wang, Y. X.; Chou, S.; Davey, K.; Dou, S. X.; Qiao, S. Z. Long-Life Room-Temperature Sodium–Sulfur Batteries by Virtue of Transition-Metal-Nanocluster–Sulfur Interactions. *Angew. Chemie., Int. Ed.* **2019**, 58 (5), 1484–1488. DOI: 10.1002/anie.201811080.
5. Ma, D.; Li, Y.; Yang, J.; Mi, H.; Luo, S.; Deng, L.; Yan, C.; Rauf, M.; Zhang, P.; Sun, X.; et al. New Strategy for Polysulfide Protection Based on Atomic Layer Deposition of TiO₂ onto Ferroelectric-Encapsulated Cathode: Toward Ultrastable Free-Standing Room Temperature Sodium–Sulfur Batteries. *Adv. Funct. Mater.* **2018**, 28 (11), 1705537. DOI: 10.1002/adfm.201705537.
6. Yang, T.; Gao, W.; Guo, B.; Zhan, R.; Xu, Q.; He, H.; Bao, S. J.; Li, X.; Chen, Y.; Xu, M. A Railway-like Network Electrode Design for Room Temperature Na-S Battery. *J. Mater. Chem. A* **2019**, 7 (1), 150–156. DOI: 10.1039/c8ta09556f.

7. Bao, W.; Shuck, C. E.; Zhang, W.; Guo, X.; Gogotsi, Y.; Wang, G. Boosting Performance of Na-S Batteries Using Sulfur-Doped Ti₃C₂T_x MXene Nanosheets with a Strong Affinity to Sodium Polysulfides. *ACS Nano* **2019**, *13* (10), 11500–11509. DOI: 10.1021/acsnano.9b04977.
8. Ma, S.; Zuo, P.; Zhang, H.; Yu, Z.; Cui, C.; He, M.; Yin, G. Iodine-Doped Sulfurized Polyacrylonitrile with Enhanced Electrochemical Performance for Room-Temperature Sodium/Potassium Sulfur Batteries. *Chem. Commun.* **2019**, *55* (36), 5267–5270. DOI: 10.1039/c9cc01612k.
9. Du, W.; Wu, Y.; Yang, T.; Guo, B.; Liu, D.; Bao, S. J.; Xu, M. Rational Construction of RGO/VO₂ Nanoflowers as Sulfur Multifunctional Hosts for Room Temperature Na-S Batteries. *Chem. Eng. J.* **2020**, *379*, 122359. DOI: 10.1016/j.cej.2019.122359.
10. Wang, L.; Chen, X.; Li, S.; Yang, J.; Sun, Y.; Peng, L.; Shan, B.; Xie, J. Effect of Eutectic Accelerator in Selenium-Doped Sulfurized Polyacrylonitrile for High Performance Room Temperature Sodium-Sulfur Batteries. *J. Mater. Chem. A* **2019**, *7* (20), 12732–12739. DOI: 10.1039/c9ta02831e.
11. Yan, Z.; Xiao, J.; Lai, W.; Wang, L.; Gebert, F.; Wang, Y.; Gu, Q.; Liu, H.; Chou, S. L.; Liu, H.; et al. Nickel Sulfide Nanocrystals on Nitrogen-Doped Porous Carbon Nanotubes with High-Efficiency Electrocatalysis for Room-Temperature Sodium-Sulfur Batteries. *Nat. Commun.* **2019**, *10* (1), 1–8. DOI: 10.1038/s41467-019-11600-3.
12. Li, Z.; Zhang, J.; Lu, Y.; Lou, X. W. A Pyrolyzed Polyacrylonitrile/Selenium

- Disulfide Composite Cathode with Remarkable Lithium and Sodium Storage Performances. *Sci. Adv.* **2018**, 4 (6), eaat1687. DOI: 10.1126/sciadv.aat1687.
13. Wei, S.; Xu, S.; Agrawal, A.; Choudhury, S.; Lu, Y.; Tu, Z.; Ma, L.; Archer, L. A. A Stable Room-Temperature Sodium-Sulfur Battery. *Nat. Commun.* **2016**, 7, 1-10. DOI: 10.1038/ncomms11722.
14. J. Wu, J.; Liu, J.; Lu, Z.; Lin, K.; Lyu, Y. Q.; Li, B.; Ciucci, F.; Kim, J. K. Non-Flammable Electrolyte for Dendrite-Free Sodium-Sulfur Battery. *Energy Storage Mater.* **2019**, 23, 8-16 DOI: 10.1016/j.ensm.2019.05.045.
15. Carter, R.; Oakes, L.; Douglas, A.; Muralidharan, N.; Cohn, A. P.; Pint, C. L. A Sugar-Derived Room-Temperature Sodium Sulfur Battery with Long Term Cycling Stability. *Nano Lett.* **2017**, 17 (3), 1863–1869. DOI: 10.1021/acs.nanolett.6b05172.
16. Augustyn, V.; Come, J.; Lowe, M. A.; Kim, J. W.; Taberna, P. L.; Tolbert, S. H.; Abruña, H. D.; Simon, P.; Dunn, B. High-Rate Electrochemical Energy Storage through Li + Intercalation Pseudocapitance. *Nat. Mater.* **2013**, 12 (6), 518–522. DOI: 10.1038/nmat3601.
17. Chen, C.; Wen, Y.; Hu, X.; Ji, X.; Yan, M.; Mai, L.; Hu, P.; Shan, B.; Huang, Y. Na⁺ Intercalation Pseudocapitance in Graphene-Coupled Titanium Oxide Enabling Ultra-Fast Sodium Storage and Long-Term Cycling. *Nat. Commun.* **2015**, 6, 1–8. DOI: 10.1038/ncomms7929.
18. Fang, Y.; Yu, X. Y.; Lou, X. W. (David). Formation of Polypyrrole-Coated Sb₂Se₃ Microclips with Enhanced Sodium-Storage Properties. *Angew. Chemie.*,

Int. Ed. **2018**, 57 (31), 9859–9863. DOI: 10.1002/anie.201805552.

19. Wang, Y.; Wang, Z.; Chen, Y.; Zhang, H.; Yousaf, M.; Wu, H.; Zou, M.; Cao, A.; Han, R. P. S. Hyperporous Sponge Interconnected by Hierarchical Carbon Nanotubes as a High-Performance Potassium-Ion Battery Anode. *Adv. Mater.* **2018**, 30 (32), 1802074. DOI: 10.1002/adma.201802074.
20. Augustyn, V.; Simon, P.; Dunn, B. Pseudocapacitive Oxide Materials for High-Rate Electrochemical Energy Storage. *Energy Environ. Sci.* **2014**, 7 (5), 1597–1614. DOI: 10.1039/c3ee44164d.
21. Li, B.; Xi, B.; Feng, Z.; Lin, Y.; Liu, J.; Feng, J.; Qian, Y.; Xiong, S. Hierarchical Porous Nanosheets Constructed by Graphene-Coated, Interconnected TiO₂ Nanoparticles for Ultrafast Sodium Storage. *Adv. Mater.* **2018**, 30 (10), 1705788. DOI: 10.1002/adma.201705788.
22. Qian, J.; Wu, F.; Ye, Y.; Zhang, M.; Huang, Y.; Xing, Y.; Qu, W.; Li, L.; Chen, R. Boosting Fast Sodium Storage of a Large-Scalable Carbon Anode with an Ultralong Cycle Life. *Adv. Energy Mater.* **2018**, 8 (16), 1703159. DOI: 10.1002/aenm.201703159.
23. Yan, J.; Li, W.; Feng, P.; Wang, R.; Jiang, M.; Han, J.; Cao, S.; Wang, K.; Jiang, K. Enhanced Na + Pseudocapacitance in a P, S Co-Doped Carbon Anode Arising from the Surface Modification by Sulfur and Phosphorus with C – S – P. *J. Mater. Chem. A* **2020**, 8, 422–432. DOI: 10.1039/c9ta11594c.
24. Zhang, J.; Shi, Y.; Ding, Y.; Peng, L.; Zhang, W.; Yu, G. A Conductive Molecular Framework Derived Li₂S/N,P-Codoped Carbon Cathode for Advanced Lithium–

Sulfur Batteries. *Adv. Energy Mater.* **2017**, 7 (14), 1602876. DOI:

10.1002/aenm.201602876.

25. Zhou, G.; Paek, E.; Hwang, G. S.; Manthiram, A. Long-Life Li/Polysulphide Batteries with High Sulphur Loading Enabled by Lightweight Three-Dimensional Nitrogen/Sulphur-Codoped Graphene Sponge. *Nat. Commun.* **2015**, 6, 1-11. DOI: 10.1038/ncomms8760.

26. Sun, J.; Sun, Y.; Pasta, M.; Zhou, G.; Li, Y.; Liu, W.; Xiong, F.; Cui, Y. Entrapment of Polysulfides by a Black-Phosphorus-Modified Separator for Lithium–Sulfur Batteries. *Adv. Mater.* **2016**, 28 (44), 9797–9803. DOI: 10.1002/adma.201602172.

27. Hu, Y.; Li, B.; Jiao, X.; Zhang, C.; Dai, X.; Song, J. Stable Cycling of Phosphorus Anode for Sodium-Ion Batteries through Chemical Bonding with Sulfurized Polyacrylonitrile. *Adv. Funct. Mater.* **2018**, 28 (23), 1801010. DOI: 10.1002/adfm.201801010.

28. Li, Y.; Yuan, Y.; Bai, Y.; Liu, Y.; Wang, Z.; Li, L.; Wu, F.; Amine, K.; Wu, C.; Lu, J. Insights into the Na + Storage Mechanism of Phosphorus-Functionalized Hard Carbon as Ultrahigh Capacity Anodes. *Adv. Energy Mater.* **2018**, 8 (18), 1702781. DOI: 10.1002/aenm.201702781.